Journal of Science: Advanced Materials and Devices 6 (2021) 462–471

Contents lists available at ScienceDirect

Journal of Science: Advanced Materials and Devices

journal homepage: www.elsevier.com/locate/jsamd

Original Article

Structural, photocatalytic and electrochemical studies on facile combustion synthesized low-cost nano chromium (III) doped polycrystalline magnesium aluminate spinels

C. Pratapkumar [a], S.C. Prashantha [b], V.G. Dileep Kumar [a], M.S. Santosh [a, *], C.R. Ravikumar [b], M.R. Anilkumar [b], T.S. Shashidhara [c], C. Nanjunda Swamy [d], A.A. Jahagirdar [e], Mir Waqas Alam [f], Zhong Chen [g], Xuan-Thanh Bui [h]

[a] Centre for Incubation, Innovation, Research and Consultancy (CIIRC), Jyothy Institute of Technology, Off Kanakapura Road, Bengaluru, 560082, Karnataka, India
[b] Research Center, Department of Science, East West Institute of Technology, Bengaluru, 560091, India
[c] Sri Siddaganga College of Arts, Science and Commerce, B.H. Road, Tumakuru, 572101, Karnataka, India
[d] Department of Civil Engineering, Ambedkar Institute of Technology, Bangalore, 560056, India
[e] Department of Chemistry, Ambedkar Institute of Technology, Bangalore, 560056, India
[f] Department of Physics, College of Science, King Faisal University, P.O. Box 400, Hofuf, Al-Hassa, 31982, Saudi Arabia
[g] School of Materials Science and Engineering, Nanyang Technological University, 50 Nanyang Avenue, 639798, Singapore
[h] Faculty of Environment and Natural Resources, University of Technology, Vietnam National University -Ho Chi Minh, Ho Chi Minh City, 700000, Viet Nam

ARTICLE INFO

Article history:
Received 11 January 2021
Received in revised form
27 May 2021
Accepted 29 May 2021
Available online 5 June 2021

Keywords:
Magnesium aluminate
Chromium dopant
Cyclic voltammetry
Acid red-88
Pyrocatechol
Emerging pollutant

ABSTRACT

An economic low-temperature self-ignition solution combustion method was used to synthesize 1–11 mol% chromium ion (Cr^{3+}) doped $MgAl_2O_4$ nanoparticles (NPs). The structural, morphological and energy gap variations due to the influence of Cr^{3+} on the host matrix were evidenced by powder X-ray diffraction (PXRD), Fourier transformed infrared spectroscopy (FTIR), diffuse reflectance spectroscopy (DRS), and transmission electron microscopy (TEM). Under visible light irradiation, the as-prepared NPs showed excellent photocatalytic activities (PCA) for the industrial dye Acid Red-88 (AR-88) and pyrocatechol (PY) - an emerging pollutant (EP). The experiments were carried out at room temperature in an aqueous solution at a concentration of 20 ppm. Among others, $MgAl_2O_4$:Cr^{3+}(5 mol%) showed 91.38% degradation within 150 min exhibiting zero-order kinetics and 82% degradation in 6 h displaying the first order kinetics for AR-88 dye and PY EP, respectively. In this case, a greater number of hydroxyl ($OH^{\cdot}$) radicles dominate over other reactive oxygen species (ROS), such as holes and singlet oxygens ($^1O_2$) under different pH conditions. Electrochemical studies have yielded the proton diffusion coefficient (D) value as large as 2.145×10^{-4} cm^2s^{-1} for the optimized NP electrode, which is substantially greater than 1.0935×10^{-5} cm^2s^{-1} for the pure $MgAl_2O_4$ one owing to the intercalated anions and structurally disordered density of the electrode material. This superior electrochemical behaviour suggests the potential application of the optimized NP material as an anodic electrode for supercapacitors.

1. Introduction

Water is a priceless nature gift for life on earth. Conservation of water should take the utmost priority but amid the growing population and industrialization, the environment is being compromised. Toxic, mutagenic and hazardous pollutants contribute significantly to water pollution through effluents coming out of food, pharmaceutical, textile, paint, paper, printing and cosmetic industries [1]. To control such heinous acts, several advanced oxidation processes (AOPs), such as adsorption, ozonation, microbial degradation, biodegradation, sonolysis, Fenton, UV/H_2O and photocatalysis have been researched and employed for the degradation of organic pollutants [2]. Azo dyes, such as acid red – 88 (AR-88) and benzene derived phenolic compounds, catechol or pyrocatechol, also known as 1,2-dihydroxybenzene are toxic organic compounds having the molecular formula $C_{20}H_{13}N_2NaO_4S$

---

* Corresponding author.
E-mail addresses: santoshgulwadi@gmail.com (M.S. Santosh), ravicr128@gmail.com (C.R. Ravikumar).

Peer review under responsibility of Vietnam National University, Hanoi.

https://doi.org/10.1016/j.jsamd.2021.05.009

and $C_6H_4(OH)_2$. High concentrations of these organic pollutants can be found in wastewater streams of many industries [3].

Currently, removal of dyes from wastewater involves various techniques like precipitation [4], flocculation/coagulation [5], biological oxidation [6], photocatalytic degradation [7], adsorption [8], membrane filtration *etc.*, [9]. Photocatalytic reaction as a chemical process that takes place under the joint action of light and the photocatalyst has shown several advantages, including environmental protection, low cost and low energy consumption for production, complete degradation of pollutants, and no secondary pollution [10].

Despite adopting the above processes, industrial wastewaters have to be treated before discharging in to the aqueous ecosystem. Effective, low-cost and reusable photocatalysts can be a solution for the water treatment on a large scale. Due to their unique physicochemical, optical and electrical properties, a wide variety of $g{-}C_3N_4$–based photocatalysts and modified TiO_2 catalysts have been designed to drive various reduction and oxidation reactions under light irradiation at appropriate wavelengths [11].

In the recent times, trivalent lanthanide rare earth (RE^{3+}) and alkali earth transition metal (TM^{3+}) oxide systems have been explored as suitable photocatalysts, for water remediation. Inorganic metal oxide nanoparticles (NPs), such as polycrystalline magnesium aluminate spinel (PMAS), $MgAl_2O_4$ *i.e.*, find a unique place in catalysis [12], because of their high mechanical strength, thermal resistance, high resistance to chemical reactions, environmental monitoring, X-ray imaging, and their optical and electrochemical properties [13–15]. Likewise, spinel structured materials play a significant role in photocatalytic and electrochemical applications, due to the presence of a large number of octahedral and tetrahedral voids. Their synthesis using a rapid combustion method is economic and has a broad spectrum of applications. In PMAS structure, both Mg^{2+} and Al^{3+}cations take one-eighth of the existing tetrahedral sites and 11/2 of the octahedral sites, so 4:3 is the general anion to cation ratio. This disorder substantially influences the photoluminescent, electrochemical and photocatalytic characters of the doped structures [16].

In this present investigation, Cr^{3+} ions doped (1–11 mol%) $MgAl_2O_4$ was prepared using a low-temperature self-ignited solution combustion process. The photocatalytic dopant concentration was optimized via a number of trails and the optimized (5 mol%) material was further studied in detail for its pH, reactive oxygen species (ROS) on AR-88 dye and PY EP. Further, the same material was analyzed for its electrochemical applications as well.

2. Experimental

2.1. Material preparation

$Mg_{(1\text{-}x)}Al_2O_4{:}xCr^{3+}$ ($x = 1–11$ mol %) NPs were prepared by an easy and fast self-ignited solution combustion synthesis (SCS) process. All the reactants were of analytical reagent (AR) grade and procured from Merck KGaA, Darmstadt, Germany. The stoichiometric amounts of magnesium nitrate hexahydrate: $Mg(NO_3)_3{\cdot}6H_2O$ (99.999%), Aluminum nitrate nonahydrate: $Al(NO_3)_3{\cdot}9H_2O$ (99.997%), Chromium (III) nitrate nonahydrate: $Cr(NO_3)_3{\cdot}9H_2O$ (99.99%), and lab made Oxalyldihydrazide (ODH): $C_2H_6N_4O_2$ were mixed thoroughly in a Petri dish via stirring using a magnetic stirrer by adding minimum amount of double distilled water for 15 min. Later, the obtained homogeneous mixture was placed inside a preheated (Temp. ~270 ± 5 °C) muffle furnace. Within a few minutes, the solution started boiling and combustion took place quickly. In the next step, the foamy product containing the dish was taken out and allowed to cool down to room temperature. The foamy white product was collected after grinding thoroughly using an agate and mortar. The complete preparation method was reported elsewhere [17].

2.2. Making of carbon paste electrode for electrochemical application

A mixture of graphite powder (99.99%), as-formed $MgAl_2O_4{:}Cr^{3+}$(5 mol%) and silicon oil were taken in the ratio 0.75:0.15:0.1. Silicon oil was added after mixing the other two ingredients. Next, the mixture was ground for about 20 min thoroughly to get a homogeneous carbon paste. The prepared paste was filled tightly onto a self-made Teflon cavity tube with high pressure to ensure good electrical contact [18].

2.3. Photocatalytic activity

Decolorization of the AR-88 dye and PY EP were performed by photocatalytic activity (PCA) experiments and their structures, which are shown in Supplementary Fig. 1. Firstly, 20 ppm of the AR-88 dye solution was prepared from the stock solution. A 250 mL aqueous solution of 20 ppm AR-88 dye and PY was taken separately, to which 0.06 g of the synthesised material was added in a 500 mL capacity circular glass reactor and reacted under a visible light source of 50 W power. The glass reactor was placed on a magnetic stirrer at a speed of 200 rpm and the stirring was allowed to run continuously throughout the experiment under open air condition [19]. The experiments on the effect of pH and scavenging were also carried out by varying the pH from acidic to basic medium (6 variations) and the appropriate scavengers, such as methanol (MeOH) as $OH^{\bullet}$ radicle, potassium iodide (KI) as hole and sodium nitride (NaN_3) as singlet oxygen ($^1O_2$) were used.

2.4. Characterization

The structural analysis was carried out using an X-ray diffractometer (Shimadzu at CuK_{α}(1.541 Å) with a scan rate of 2° per minute. The functional groups in the prepared materials were identified using a PerkinElmer FTIR spectrometer (Spectrum-1000) in the range of 4000–400 cm^{-1}. The morphology, polycrystallinity and interplanar distance were determined using a JEOL transmission electron microscope (TEM) (JEM-2100 with accelerating voltage up to 200 kV, LaB_6 filament)). To calculate the energy bandgap, the K-M function was used. The diffuse reflectance spectral (DRS) studies were performed to calculate the energy band gap using the Shimadzu UV–Vis spectrophotometer model 2600 in the range of 200–800 nm. Electrochemical Impedance studies were performed on an Electrochemical Analyzer (CH Instruments model-608E) having a three-electrode system.

3. Results and discussion

3.1. Structural studies

Fig. 1(a) shows the PXRD spectra of the combustion synthesized $MgAl_2O_4$ NPs, as formed at 270 ± 5 °C. The XRD peaks indicate that the prepared materials ($MgAl_2O_4{:}Cr^{3+}$(1 mol%) to $MgAl_2O_4{:}Cr^{3+}$(11 mol%)) were of a typical cubic structured crystalline spinel material and all the identified planes (111), (220), (311), (222), (440), (422), (511), (440), (531), (620) and (533) are in good agreement with the JCPDS No. 21–1152 with space group $Fd\bar{3}m$ (O_h^7, No. 227).

It is also worthy to note that no impurity peaks were found, indicating a homogeneous doping of Cr^{3+} cations to the host crystal lattice in the sites of Mg^{2+} ($R_{Cr}^{3+} = 0.052$ nm and $R_{Mg}^{2+} = 0.072$ nm)

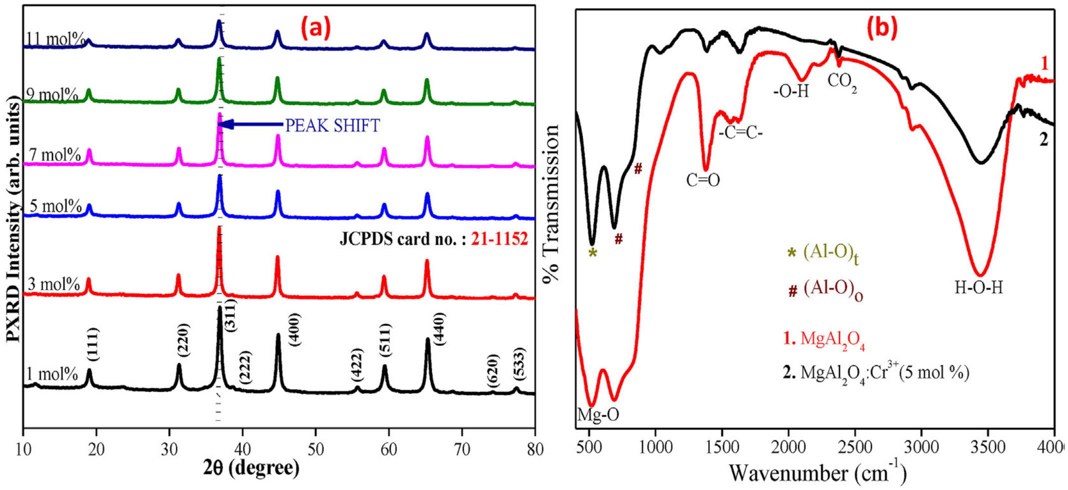

Fig. 1. (a) PXRD patterns of $MgAl_2O_4:Cr^{3+}$ (1–11 mol %) nano powders at low temperature 270 °C± 5 °C with lower angle peak shift indications. (b) Comparison of FT-IR spectra of $MgAl_2O_4$ and $MgAl_2O_4:Cr^{3+}$(5 mol%).

[20]. On comparing the XRD patterns of all the materials, the peak shift is significant and it is due to the increase in the Cr^{3+} dopant concentration, which may cause the micro strains to develop in the host lattice. The crystal plane (311) was considered to find the mean crystallite size (D), which was estimated between 12 and 20 nm as obtained from the Scherrer's equation [21].

The FTIR spectra of pure $MgAl_2O_4$ and $MgAl_2O_4:Cr^{3+}$(5 mol%) were taken between 400 and 4000 cm^{-1} by making KBr sample pellets (Fig. 1(b)). The peaks between 400 and 900 cm^{-1} are due to Al—O (asymmetric stretching at 850 cm^{-1}), Mg—O (670 cm^{-1}), Al—O (Metal—Oxygen) (530 cm^{-1}) and MgO_6 octahedral (440 cm^{-1}) stretching modes [28]. The H—O—H bending vibration peak at 1700 cm^{-1} and O—H stretching vibration peak at 3350 cm^{-1} could be assigned to small amounts of H_2O molecules. The stretching bonds of C=O, C=C were assigned in the range 1400–1600 cm^{-1}. The ~2300 cm^{-1} peak was attributed to the absorption of atmospheric CO_2 by the Al and Mg cations [22,23].

The diffuse reflectance spectra (Fig. 2) show wide absorption bands at 556 nm ($^4A_{2g}(F) \rightarrow {}^4T_{2g}(F)$) and 375 nm ($^4A_{2g}(F) \rightarrow {}^4T_{1g}(F)$) that come from the spin allowed d→d transitions of octahedral chromium ions present in the $MgAl_2O_4$. The E_g (energy band gap) was calculated by K-M function (Kubelka—Munk) f(R) as discussed elsewhere [24]. The inset of Fig. 2 shows the plot of $f(R)^2$ versus E_g. The extrapolation of the curves resulted in the E_g values of $MgAl_2O_4$(4.5eV) and $MgAl_2O_4:Cr^{3+}$(3.7 eV), which indicate the change in the energy band gap due to the dopant chromium ion in the host material [25].

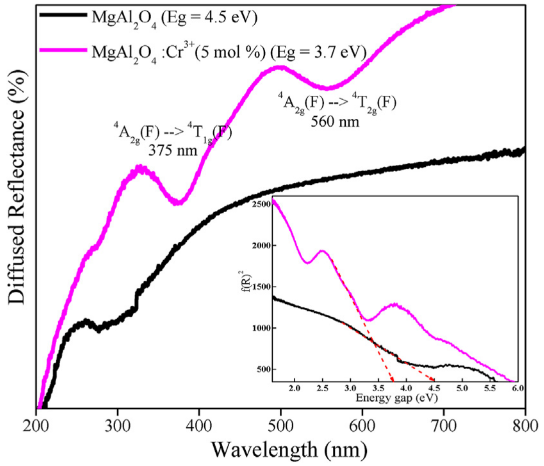

Fig. 2. DRS and energy gap spectra of the as-formed $MgAl_2O_4$ and $MgAl_2O_4:Cr^{3+}$(5 mol %).

Fig. 3(a) shows the transmission electron microscopic (TEM) image of the prepared $MgAl_2O_4$ nanocrystal, and the average size of the NPs was found to be between 15 and 25 nm, as calculated from Scherer's formula. The selected area electron diffraction (SAED) pattern indicates the polycrystallinity of the material showing concentric rings representing the crystal planes (Fig. 3(b)). With the help of high-resolution TEM (HR-TEM) (Fig. 3(c)), the fringe width value (d = 0.495 nm) for the (311) plane was found which is close to the theoretical value of 0.5 nm. Energy dispersive X-Ray (EDX) composition analysis (see Fig. 3(d)) shows the elemental compositions (Mg, Al and O) along with the copper grid composition Cu, which can be neglected [26].

3.2. Photocatalytic studies on AR-88 dye and PY

The photocatalytic studies of the prepared $MgAl_2O_4:Cr^{3+}$ were performed to see the degradation efficiency of AR-88 dye and PY in an aqueous medium under the irradiation of visible light with variable parameters, such as exposing time, pH and scavengers using UV absorption spectroscopy.

Supplementary Fig. 2. shows the UV-Visible absorption spectra (350–600 nm) for the 20ppm AR-88 solution at a time interval of every 15 min up to 150 min. Likewise, all the prepared materials of $MgAl_2O_4:Cr^{3+}$(0–11 mol%) were studied for their degradation efficiency. The primary observation was that the decolorization first increased with an increase in Cr^{3+} concentration from 1 to 5 mol%, and then decreased with a further increase in the doping concentration (Fig. 4(a)). The transition metal Cr^{3+} ions on the surface of $MgAl_2O_4$ host act as an electron trapper to isolate the electron—hole pairs which are beneficial for photocatalytic response. In other words, 5 mol% Cr doping exhibits superior PCA *i.e.*, 91.38% degradation (Fig. 4(b)) and this may be due to the high efficiency of the separation of electron—hole pairs [27]. Fig. 4(c) depicts half-life time ($T_{1/2}$) plot (lnC/Co and C/Co *vs* time) which shows that the optimized photocatalyst can degrade half of the dye present in the dye solution within 65.24 min. Fig. 4(d) indicates the % removal of the total organic carbon (TOC) present in the dye solution in 150 min and the TOC was observed to be 82%.

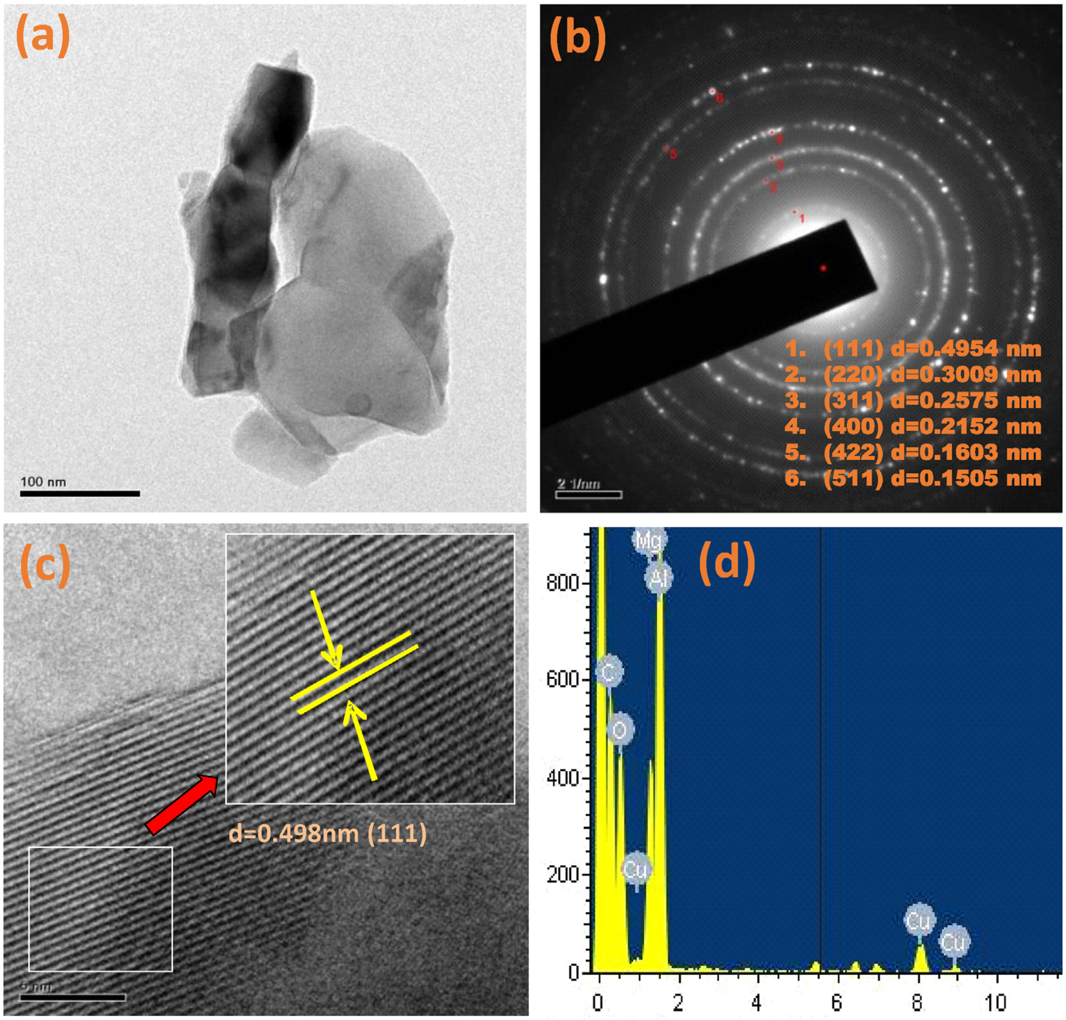

Fig. 3. (a) TEM image, (b) SAED, (c) HRTEM and (d) EDAX spectra of $MgAl_2O_4$.

Under the visible light irradiation, holes act as charge carriers from the valence band (VB) to the conduction band (CB) and the scavenging radicals are strong oxidants that can cause photocatalysis [28]. In the photocatalytic process, Cr^{3+} cations receive electrons in the CB of the host to form Cr^{3+} which in turn transfers an electron to the dissolved O_2 and turns it into superoxide radical anions resulting in the light induced electron - hole recombinations. The optimized material, $MgAl_2O_4:Cr^{3+}$ (5 mol%), was considered for the PY degradation. Both the catalysis works have been discussed in detail below.

3.2.1. Effect of pH on photocatalytic activity

Fig. 5 (a) and (b) show the effect of pH and scavengers on the AR-88 dye. The solution pH was varied from acidic (pH-3) to basic medium (pH-13) under visible light irradiation for the mentioned duration. The degradation percentage was calculated and represented in Fig. 5 (c) and (d), and it is noted that the acidic medium (the initial pH-3) was supportive for the degradation. The degradation was maximum in the basic medium (pH-13) [28], and was further confirmed by the scavenging studies that the photocatalyst was producing more amounts of hydroxyl (OH) radicals. The correlation between the degradation (%) and variable pH of the solution was found to be significant as the R^2 value was almost equals to 1 (Table 1).

Fig. 6 (a) and (b) show the effect of pH on the PY degradation by changing the solution pH from acidic (pH-2) to basic (pH-12) for PCA under the similar conditions as discussed above with a time interval of 1 h up to 6 h. The degradation percentage was calculated and represented in Fig. 6 (c) and (d). It is observed that the initial pH (pH-6) was supportive for degradation and degraded up to 82% in 6 h and the degradation decreased as the solution approached acidic pH. Whereas, in a basic medium, the degradation was observed to be maximum as the photocatalyst produced a greater number of $OH^{\cdot}$ radicals. The production of $OH^{\cdot}$ by the photocatalyst was further confirmed by the scavenging action of MeOH [29–31]. The correlation between the degradation (%) and variable pH of the solution was found to be significant as the R^2 value was almost equal to 1 (Table 2).

3.2.2. Kinetic of photocatalytic degradation

The degradation of AR-88 dye and PY using the optimized photocatalyst under visible light irradiation exhibits a zero-order reaction (Supplementary Fig. 3. (a & b)) and a first order reaction (Supplementary Fig. 3. (c & d)), respectively. The rate constant relation for the zero-order and first-order reactions is as follows:

$$C - C_o = -kt \tag{1}$$

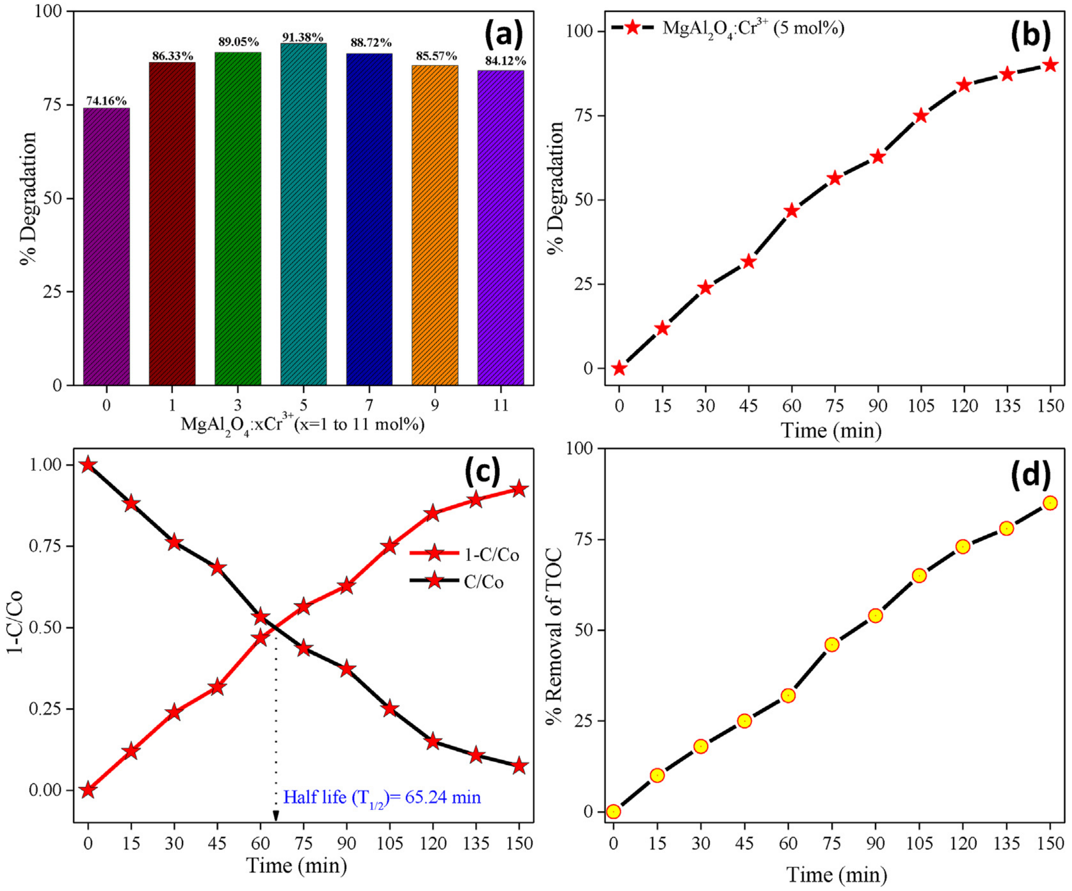

Fig. 4. (a) Degradation (%) of AR-88 dye *vs* Cr^{3+}concentration in $MgAl_2O_4$; (b) Plot of %D *vs* time; (c) Half-life ($T_{1/2}$) plot; (d) Plot of % removal of TOC for $MgAl_2O_4$:Cr^{3+}(5 mol%) dye.

$$\ln\frac{C}{C_0}=kt \tag{2}$$

where C is the final concentration, C_0 is the initial concentration, t is the time interval and k is the rate constant for the zero-order (Z-O) and the first-order (F—O) reaction. The plot of concentration *vs* time shows a linear curve for Z-O reaction ($R^2 = 0.99947$ at pH-13) and the plot of ln C *vs* time shows the F—O reaction ($R^2 = 0.99993$ at pH-6) for AR-88 dye and PY EP, respectively.

The kinetic values show a good linear fit of the Z-O reaction (AR-88) and F—O reaction (PY EP). The values of the rate constant k and R^2 values are given in Tables 1 and 2 [32,33].

3.2.3. Scavengers studies

To determine the reactive oxygen species (ROS) during the dye degradation, scavenging experiments were performed using sodium nitride (NaN_3), potassium iodide (KI) and methanol (MeOH) as the singlet oxygen scavenger ($^{1}O_2$), hole scavenger and •OH radical scavenger respectively. For AR-88 dye and PY, the plot of degradation (%) *vs* pH/scavengers was plotted and after the addition of scavengers, MeOH, KI and NaN_3, the degradation of AR-88 dye was found to be 85.18, 30 and 20.11%, respectively, and 14.34, 68.50 and 79.82%, respectively, for the PY. From these results, we can conclude that the photocatalyst produces greater number of OH radicals and the degradation efficiency of the photocatalyst at different pH values shows the action of these radicals in the order of the $^{\circ}$OH > $^{1}O_2$> hole [34,35].

3.2.4. Reusability of the photocatalyst up to 5 cycles

Reusability studies were done under visible light up to 900 min and 36 h at same time intervals for AR dye and PY degradation. After the first cycle ($n = 1$) of the photocatalytic experiment, the photocatalyst was separated from the degraded solution by centrifugation, and it was washed thoroughly with water and ethanol followed by drying (at 80 °C) before the next consecutive cycles. For AR-88 dye (Fig. 7(a)) and PY (Fig. 7(b)), after 5 cycles ($n = 5$) of reusability testing, the degradation decreased by 24.38% (91.38%–67%) and 6% (82%–76%). This clearly concludes that the prepared material could be an effective recyclable photocatalyst and can be effectively used in practical applications under visible light irradiation [36].

3.3. Cyclic voltammetry and electrochemical impedance studies

Cyclic voltammetry (CV) measurements of the electrode prepared from pure $MgAl_2O_4$ and $MgAl_2O_4$:Cr^{3+} (5 mol %) nano powders were carried out to study their electrochemical properties. Fig. 8 (a and b) shows the cyclic voltammograms of the undoped and Cr^{3+} (5 mol %) doped $MgAl_2O_4$ electrodes, respectively. A three-electrode system was incorporated and the prepared carbon paste electrode was used as the working electrode, Ag/AgCl as the reference and platinum as the counter electrode. To know the oxidation and reduction peaks in the material, voltage was applied in the range between −1.6 and 0.4 V. The CV plot clearly shows a reduction peak and an oxidation peak at several stages in the rate system. The pseudo capacitance could be one of the reasons for the

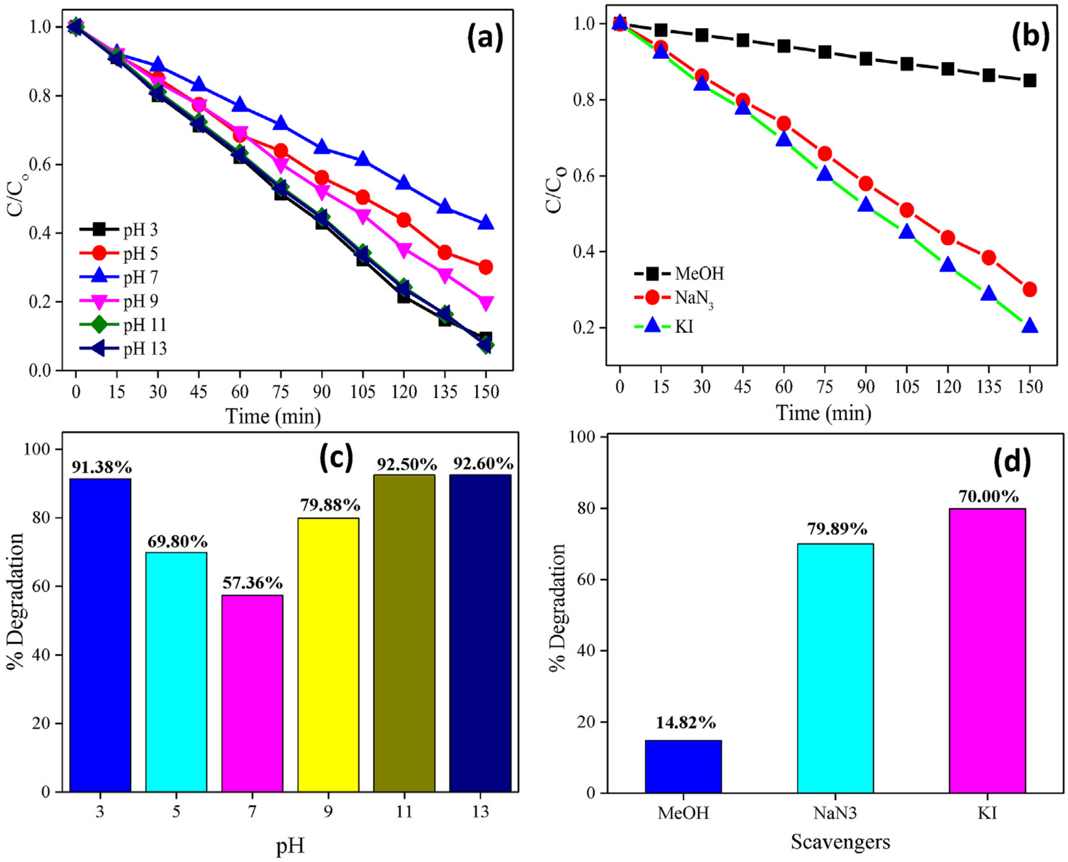

Fig. 5. Effect of pH (a & c) and Scavengers (b & d) on degradation of AR-88 dye.

Table 1
Rate constant k and R^2 values of zero order reaction of AR-88 dye degradation.

pH							Scavengers		
	3	5	7	9	11	13	MeOH	NaN_3	KI
R^2	0.99695	0.9974	0.99774	0.99928	0.99963	0.99947	0.99937	0.99907	0.99951
k	0.12506	0.09319	0.07583	0.10695	0.1246	0.1241	0.01994	0.09357	0.10664

above performance and this shows that the actual capability of the working electrode is primarily based on the redox mechanism [37].

The peak current in the reversible method can be expressed as i_p in steps with the R–S (Randles-Sevcik) relation [38] as shown below:

$$i_p = 2.69x\ 10^5 \times n^{3/2} \times A \times D^{1/2} \times C_0 \times v^{1/2} \tag{3}$$

$$C_0 = \frac{\rho}{M} \tag{4}$$

where n, A, D, v and C_0 are the number of transferred electrons as a response to the electrode extent, the diffusion co-efficient, the rate of scanning and the initial concentration of the chemical estimated for the prepared electrode (Eq. (4)) using the theoretical density (ρ) and molar mass (M), respectively.

The linearity in the cathodic peak current (i_p) versus square root of the scan rate ($\nu^{1/2}$) plot (Fig. 8(c)) shows that the electrode responses of the pure and Cr doped samples were confined. The value of the proton diffusion coefficient (D) was found by the slope value, which was calculated for both the electrode materials as 2.145×10^{-4} cm^2s^{-1} for $MgAl_2O_4:Cr^{3+}$(5 mol%), and this was comparatively greater than 1.0935×10^{-5} cm^2s^{-1} for pure $MgAl_2O_4$, owing to intercalated anions and structural disorder density of the electrode material.

Electrochemical impedance spectroscopy (EIS) estimation was carried out for the prepared electrode material to assess the ion diffusion and the electrical conductivity. This result explains the easier penetration of the electrolyte medium via the prepared electrode material clarifying the areal capacitance as discussed below.

EIS measurements were recorded in the range of 1Hz to 1 MHz frequency at an open circuit potential (OCP) with 10 mV AC excitation. Fig. 9 (a) shows the Nyquist plot of $MgAl_2O_4$ and Cr doped (5 mol%) $MgAl_2O_4$ electrode. In this plot, Real (Z') and Imaginary (Z'') components relate to ohmic and capacitive properties, respectively.

Warburg part (W) lies in the lower frequency side of the Z' *vs* Z'' spectra. Q_1 and Q_2 are the constants that are parallel to the charge transfer resistance (R_{ct}) and the low-frequency capacitance and are also parallel to the outflow resistance (R_l).

In these plots, a crescent structure in the region of elevated frequencies and a close line inside the short frequency zone can be noticeable at a distance that the line in the low-frequency regime

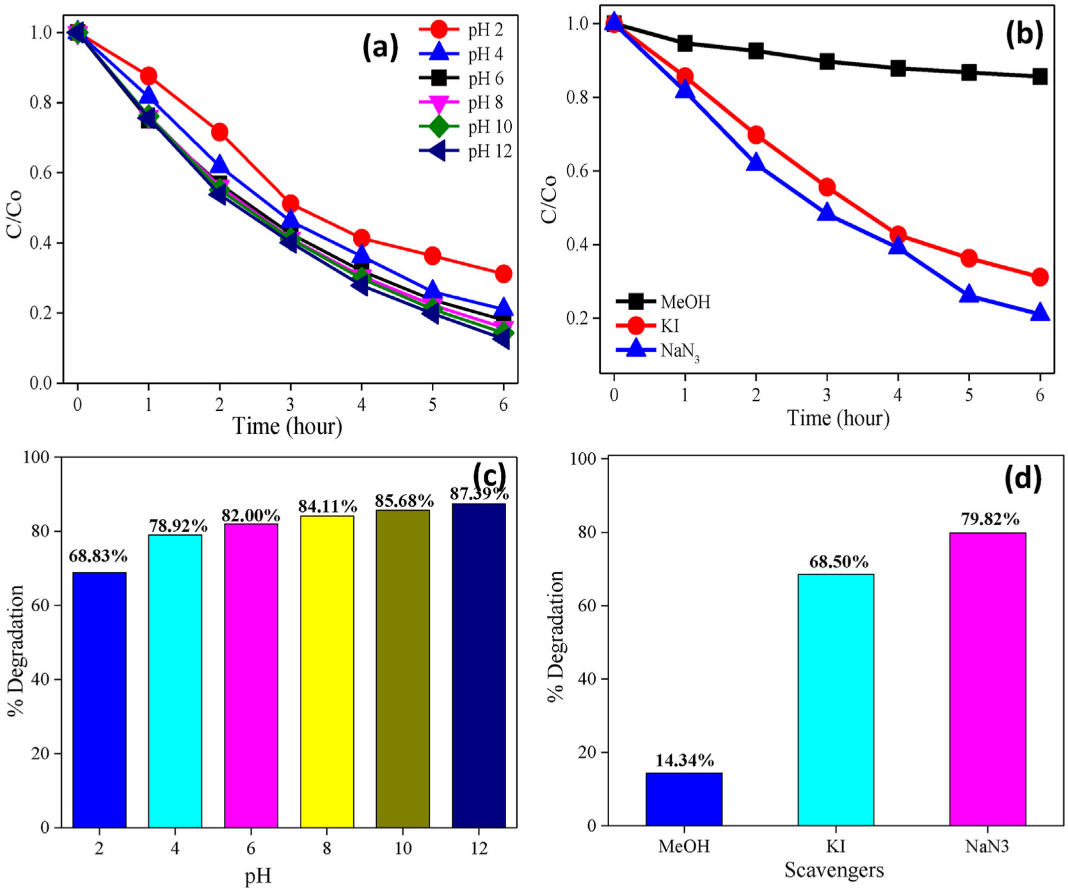

Fig. 6. Effect of pH (a & c) and Scavengers (b & d) on degradation of PY EP.

Table 2
Rate constant *k* and R^2 values of first order reaction of PY EP degradation.

pH							Scavengers		
	2	4	6	8	10	12	MeOH	NaN$_3$	KI
R^2	0.97977	0.99717	0.99993	0.99911	0.99695	0.9947	0.93255	0.99213	0.98431
k	0.477	0.6098	0.6594	0.7069	0.74151	0.78539	0.05666	0.6095	0.4692

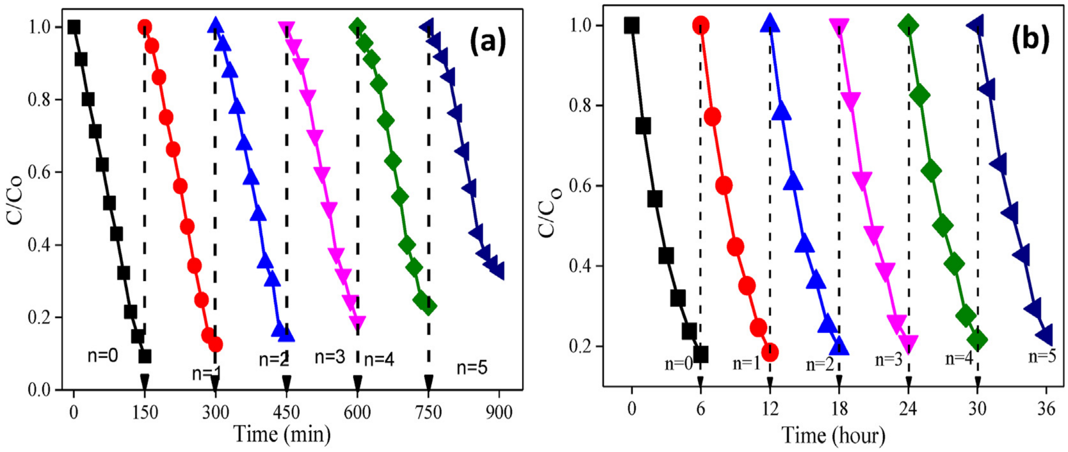

Fig. 7. Reusability of photocatalyst with (a) AR-88 dye and (b) PY.

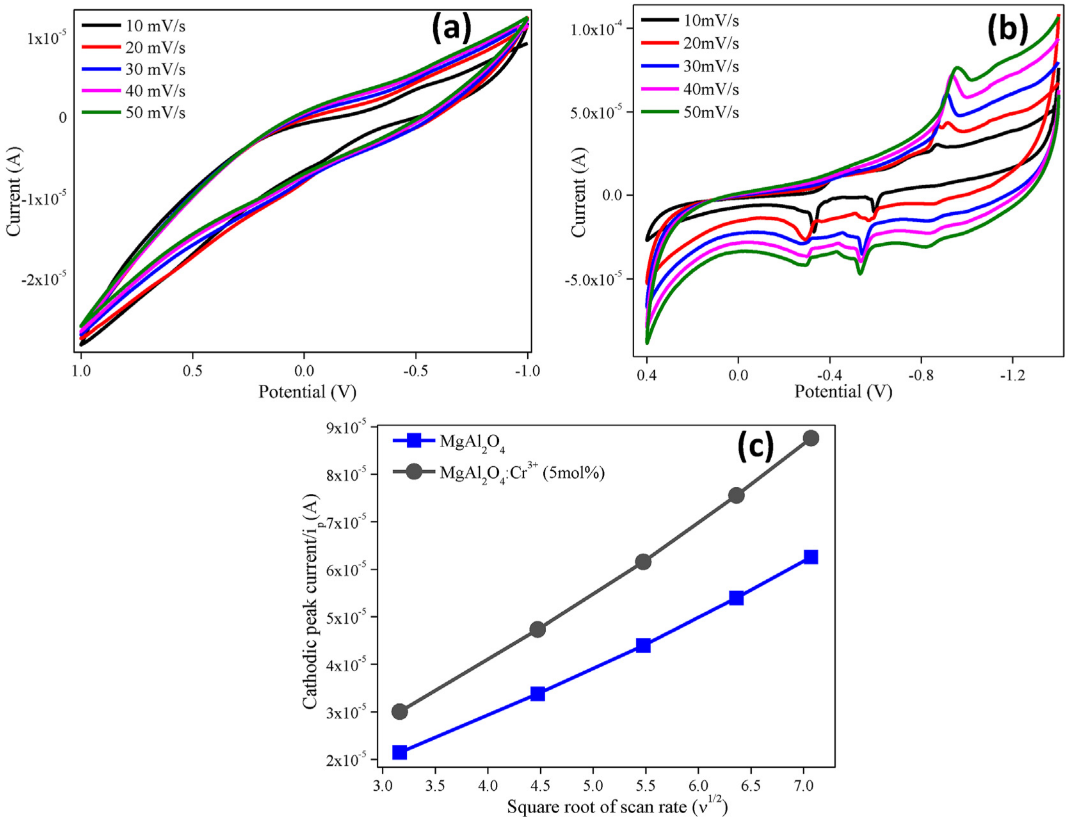

Fig. 8. Cyclic voltammogram of (a) $MgAl_2O_4$, (b) $MgAl_2O_4$:Cr^{3+}(5 mol%) electrode and **(c)** Relationship between the cathodic peak current (ip) and the square root of the scan rate ($v^{1/2}$) of $MgAl_2O_4$ and $MgAl_2O_4$:Cr^{3+}(5 mol%) electrode.

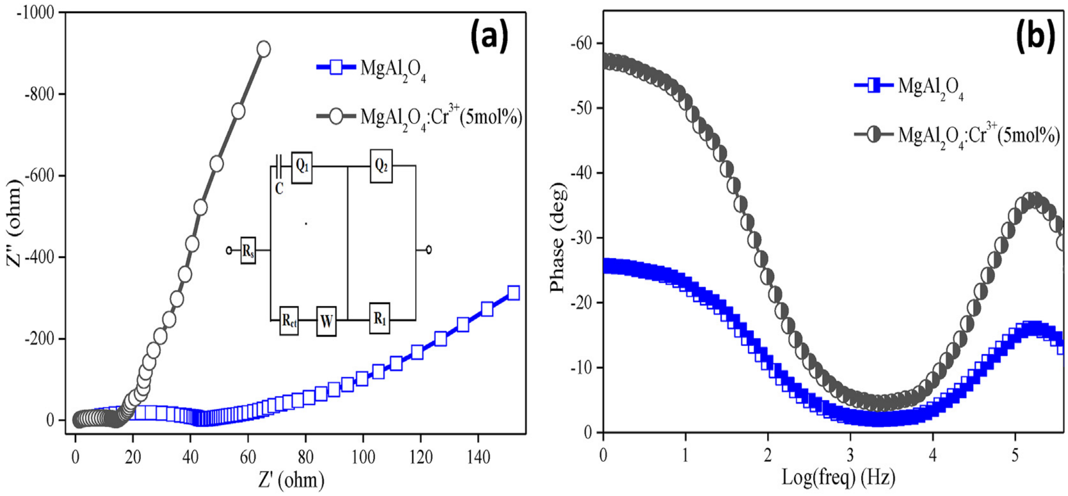

Fig. 9. (a) Nyquist plot of $MgAl_2O_4$ and Cr doped (5 mol%) $MgAl_2O_4$ electrode with equivalent Circuit (Inset). **(b)** Bode plot of $MgAl_2O_4$ and Cr-doped $MgAl_2O_4$ electrodes.

displays the diffusion resistance of the electrolyte ions inside the electrode structures and the exorbitant frequency curve equivalences to the resistance from the charge transfer (R_{ct}) over the electrolyte–electrode edge. Normally, semicircles with larger radii denotes an advanced electrode charge transfer resistance. Further, the inferior value 'R_{ct}' of $MgAl_2O_4$:Cr^{3+} (5 mol %) can be because of their lesser nanostructures which are formed with over-the-top thickness, offering a high surface locale and a simple way for the de-intercalation and intercalation of the electrolyte ions, which could effectively reduce the internal resistance of the material. The R_S, R_{ct}, C_{dl}, Q_1 and Q_2 values were obtained by fitting the equivalent circuits (Fig. 9(a)) for the impedance spectra of pure and Cr^{3+} (5 mol %) doped $MgAl_2O_4$ electrodes (Table 3). Bode plot demonstrated in Fig. 9(b) clarifies the connection between the phase angle and frequency, *i.e.*, the phase angle is −57°, which is enhanced towards the value of the ideal capacitor (−90°), but the phase angle of the undoped $MgAl_2O_4$ electrode material was found to be −26°, which was far away from an ideal capacitor [39].

Table 3
The charge transfer resistance (R_{ct}) and double layer capacitance (C) value of $MgAl_2O_4$ and $MgAl_2O_4$:Cr^{3+} (5 mol%).

Electrode $MgAl_2O_4$:xCr^{3+}	R_S (Ω)	R_{Ct}(Ω)	C_{dl} (F)	Q_1 (rad/S)	Q_2 (F)
$x = 0$ mol%	3.292	42.56	3.840×10^{-6}	0.5308	0.6856
$x = 5$ mol%	1.374	17.18	2.508×10^{-4}	0.9905	0.9996

4. Conclusion

The $MgAl_2O_4$:Cr^{3+} (1–11 mol %) nanoparticles were successfully prepared via the solution combustion method. The PXRD patterns confirm that the synthesized NPs show a cubical structure with a crystallite size of ~15 nm matching with the TEM results. Among all the prepared materials, $MgAl_2O_4$:Cr^{3+}(5 mol%) shows the highest degradation percentage (91.38% and 82%) in a time span of 150 min and 6 h, exhibiting the zero order and first order kinetics for AR-88 dye (20 ppm) and PY (20 ppm), respectively, under visible light irradiation. Among the scavengers used, the reactions produced more OH· radicals compared to the holes and the singlet oxygen in the photocatalytic activity under varied pH environments. EIS studies show a high charge transfer resistance and high reversible electrode reaction for the MgAl2O4:Cr^{3+}(5 mol%) electrode material. All the above outcomes signify that the synthesized nanomaterial can be effectively used as a photocatalyst for water treatment and also as a supercapacitor for energy storage applications.

Declaration of competing interest

The authors declare that they have no known competing financial interests or personal relationships that could have appeared to influence the work reported in this paper.

Acknowledgements

This work was supported by the Science and Engineering Research Board, Govt. of India under the ASEAN - India Collaborative R&D Scheme (Project Grant No. CRD/2018/000066 M.S.S) of the ASEAN - India S&T Development Fund (AISTDF). Further, the authors wish to thank the Research Center - East West Institute of Technology, Bengaluru, Center for Incubation, Innovation, Research and Consultancy (CIIRC) - Jyothy Institute of Technology for extending their support to carry out this research work.

Appendix A. Supplementary data

Supplementary data to this article can be found online at https://doi.org/10.1016/j.jsamd.2021.05.009.

References

[1] A. Gogoi, M. Navgire, K.C. Sarma, P. Gogoi, Fe_3O_4-CeO_2 metal oxide nanocomposite as a Fenton-like heterogeneous catalyst for degradation of catechol, Chem. Eng. J. 311 (2017) 153–162.

[2] M. Ahmadi, B. Kakavandi, S. Jorfi, M. Azizi, Oxidative degradation of aniline and benzotriazole over PAC@ FeIIFe$_2$IIIO$_4$: a recyclable catalyst in a heterogeneous photo-Fenton-like system, J. Photochem. Photobiol., A: Inside Chem. 336 (2017) 42–53.

[3] A.A. Aghapour, G. Moussavi, K. Yaghmaeian, Degradation and COD removal of catechol in wastewater using the catalytic ozonation process combined with the cyclic rotating-bed biological reactor, J. Environ. Manag. 157 (2015) 262–266.

[4] M.X. Zhu, Li Lee, H. H Wang, Z. Wang, Removal of an anionic dye by adsorption/precipitation processes using alkaline white mud, J. Hazard Mater. 149 (2007) 735–741.

[5] M. Yousuf, A. Mollah, R. Schennach, J.R. Parga, L.C. David, Electro coagulation (EC) -science and applications, J. Hazard Mater. 84 (2001) 29–41.

[6] N.T. Thao, H.D.K. Nguyen, Advanced oxidation of Rhodamine-B with hydrogen peroxide over Zn–Cr layered double hydroxide catalysts, J. Sci.: Adv. Mater. Devices 2 (2017) 317–325.

[7] M.R. Anil Kumar, B. Abebe, H.P. Nagaswarupa, H.C. Ananda Murthy, C.R. Ravikumar, Fedlu Kedir Sabir, “Enhanced photocatalytic and electrochemical performance of TiO_2-Fe_2O_3 nanocomposite: its applications in dye decolorization and as supercapacitors”, Nature 10 (2020) 1249. Scientific Reports.

[8] M. Salleh, D.K. Mahmoud, W. Karim, A. Idris, Cationic and anionic dye adsorption by agricultural solid wastes: a comparative review, Desalination 280 (2011) 1–13.

[9] S. Sharma, A. Kaur, Various methods for removal of dyes from industrial effluents - a review, Indian J. Sci. Technol. (2018) 11.

[10] V.G. Dileepkumar, P.S. Surya, C. Pratapkumar, R. Viswanatha, C.R. Ravikumar, M.R. Anil Kumar, H.B. Muralidhara, Islam M. Al-Akraa, Ahmad M. Mohammad, Zhong Cheng, Xuan-Thanh Buih, Mysore Sridhar Santosh, $NaFeS_2$ as a new photocatalytic material for the degradation of industrial Dyes, J. Environ. Chem. Eng. 8 (2020) 104005.

[11] J. Wen, J. Xie, X. Chen, X. Li, A review on g-C_3N_4-based photocatalysts, Appl. Surf. Sci. 391 (2017) 72–123.

[12] R.C. Ropp, Luminescence and the Solid State. Studies in Inorganic Chemistry, second ed., 2004, p. 21.

[13] M.R. Anilkumar, H.P. Nagaswarupa, K.S. Anantharaju, K. Gurushantha, C. Pratapkumar, S.C. Prashantha, T.S. Shekhar, H. Nagabhushana, S.C. Sharma, Y.S. Vidya, D. Prasad, Green engineered ZnO nanopowders by Banyan Tree and E. tirucalli plant latex: auto ignition route, photoluminescent and photocatalytic properties, Mate. Resea. Expr. 2 (2015), 035011.

[14] W. Luo, P. Ma, T. Xie, J. Dai, Y. Pan, H. Kou, J. Li, Fabrication and spectroscopic properties of Co: $MgAl_2O_4$ transparent ceramics by the HIP post-treatment, Optic. Mater 69 (2017) 152–157.

[15] P. Głuchowski, R. Pązik, D. Hreniak, W. Stręk, Luminescence studies of Cr^{3+} doped $MgAl_2O_4$ nanocrystalline powders, Chem. Phys. 358 (2009) 52–56.

[16] B.P. Uberuaga, D. Bacorisen, R. Smith, J.A. Ball, R.W. Grimes, A.F. Voter, K.E. Sickafus, Defect kinetics in spinels: long-time simulations of $MgAl_2O_4$, $MgGa_2O_4$, and $MgIn_2O_4$, Phys. Rev. B 75 (2007) 104–116.

[17] B.P. Uberuaga, D. Bacorisen, R. Smith, J.A. Ball, R.W. Grimes, A.F. Voter, K.E. Sickafus, Defect kinetics in spinels: long-time simulations of $MgAl_2O_4$, $MgGa_2O_4$, and $MgIn_2O_4$, Phys. Rev. B. 75 (2007) 104116.

[18] Aarti S. Bhatt, R. Ranjitha, M.S. Santosh, C.R. Ravikumar, S.C. Prashantha, Rapela R. Maphanga, Guilherme F.B. Lenz e Silva, Optical and electrochemical applications of Li-doped NiO nanostructures synthesized via facile microwave technique, Materials 13 (2020) 2961.

[19] W.A.I. Tabaza, H.C. Swart, R.E. Kroon, Luminescence of Ce doped $MgAl_2O_4$ prepared by the combustion method, Phys. B Condens. Matter 439 (2014) 109–114.

[20] C. Pratapkumar, S.C. Prashantha, H. Nagabhushana, M.R. Anilkumar, C.R. Ravikumar, H.P. Nagaswarupa, D.M. Jnaneshwara, White light emitting magnesium aluminate nanophosphor: near ultra violet excited photoluminescence, photometric characteristics and its UV photocatalytic activity, J. Alloys Compd. 728 (2017) 1124–1138.

[21] D. Chikte, S.K. Omanwar, S.V. Moharil, Luminescence properties of red emitting phosphor $NaSrBO_3$: Eu^{3+} prepared with novel combustion synthesis method, J. Luminescence 142 (2013) 180–183.

[22] M.R.A. Kumar, H.P. Nagaswarupa, K.S. Anantharaju, K. Gurushantha, C. Pratapkumar, S.C. Prashantha, T.R. Shashishekar, H. Nagabhushana, S.C. Sharma, Y.S. Vidya, B.D. Prasad, C.S.V. Babu, K.R.V. Mahesh, Banyan latex: a facile fuel for the multifunctional properties of MgO nanoparticles prepared via auto ignited combustion route, Mater. Res. Express 2 (2015), 095004.

[23] H. Shahbazi, H. Shokrollahi, A. Alhaji, Optimizing the gel-casting parameters in synthesis of $MgAl_2O_4$ spinel, J. Alloys Compd. 712 (2017) 732–741.

[24] C. Pratapkumar, S.C. Prashantha, H. Nagabhushana, D.M. Jnaneshwara, Photoluminescence and photometric studies of low temperature prepared red emitting $MgAl_2O_4$:Cr^{3+} nanophosphors for solid state displays, J. Scien. Adv. Mater. Devi. 3 (2018) 464–470.

[25] C. Shivakumara, R. Saraf, S. Behera, N. Dhananjaya, H. Nagabhushana, Synthesis of Eu3+-activated BaMoO4 phosphors and their Judd–Ofelt analysis: applications in lasers and white LEDs, Spectrochim. Acta, Part A: Mol. Bio. Spec. 151 (2015) 141–148.

[26] M. Shivram, S.C. Prashantha, H. Nagabhushana, S.C. Sharma, K. Thyagarajan, R. Harikrishna, B.M. Nagabhushana CaTiO, Eu^{3+} red nanophosphor: low temperature synthesis and photoluminescence properties, Spectrochim. Acta, Part A: Mol. Biom. Spectr. 120 (2014) 395–400.

[27] R. Naik, S.C. Prashantha, H. Nagabhushana, S.C. Sharma, H.P. Nagaswarupa, K.S. Anantharaju, D.M. Jnaneshwara, K.M. Girish, Tunable white light emissive Mg_2SiO_4:Dy^{3+} nanophosphor: its photoluminescence, Judd–Ofelt and photocatalytic studies, Dyes Pigments 127 (2016) 25–36.

[28] L. Chen, X. Jiang, R. Xie, Y. Zhang, Y. Jin, W. Jiang, A novel porous biochar-supported Fe-Mn composite as a persulfate activator for the removal of acid red 88, Separ. Purif. Technol. (2020) 117232.

[29] U.B. Deshannavar, P.K. Singa, D. Gaonkar, A. Gayathri, A. Patil, L.V. Malade, Removal of acid violet 49 and acid red 88 dyes from aqueous solutions using advanced oxidation process, Mate. Toda. Proce. 24 (2020) 1011–1019.

[30] M. Ahmadi, B. Kakavandi, N. Jaafarzadehand, A.A. Babaei, Catalytic ozonation of high saline petrochemical wastewater using PAC@FeIIFe$_2$IIIO$_4$: optimization, mechanisms and biodegradability studies, Separ. Purif. Technol. 177 (2017) 293–303.

[31] H. Ferkous, S. Merouani, O. Hamdaoui, C. Pétrier, Persulfate-enhanced sonochemical degradation of naphthol blue black in water: evidence of sulfate radical formation, Ultrason. Sonochem. 34 (2017) 580–587.

[32] I. Epold, M. Trapido, N. Dulova, Degradation of levofloxacin in aqueous solutions by Fenton, ferrous ion-activated persulfate and combined Fenton/persulfate systems, Chemi. Eng. J. 279 (2015) 452–462.

[33] M.H. Nejad, A. Takdastan, N. Jaafarzadeh, M.A. Mogadam, N. Mengelizadeh, Removal of orthophosphate from municipal wastewater using chemical precipitation process in Ahvaz wastewater treatment plant, Iran. Asia, J. Chem. 25 (2013) 2565.

[34] A. Ghauch, A.M. Tuqan, N. Kibbi, S. Geryes, Methylene blue discoloration by heated persulfate in aqueous solution, Chem. Eng. J. 213 (2012) 259–271.

[35] A. Long, Y. Lei, H. Zhang, Degradation of toluene by a selective ferrous ion activated persulfate oxidation process, Indus. Engine. Chem. Res. 53 (2014) 1033–1039.

[36] R. Marquez, J. José, I. Levchuk, P.F. Ibañez, M. Sillanpää, A critical review on application of photocatalysis for toxicity reduction of real wastewaters, J. Clean. Prod. (2020) 120694.

[37] C.R. Ravikumar, M.S. Santosh, H.P. Nagaswarupa, S.C. Prashantha, S. Yallappa, M.R.A. Kumar, Synthesis and characterization of β-Ni$(OH)_2$ embedded with MgO and ZnO nanoparticles as nanohybrids for energy storage devices, Mater. Res. Express 40 (2017) 65503.

[38] C.R. Ravikumar, M.R.A. Kumar, H.P. Nagaswarupa, S.C. Prashantha, A.S. Bhatt, M.S. Santosh, D. Kuznetsov, CuO embedded β-Ni$(OH)_2$ nanocomposite as advanced electrode materials for supercapacitors, J. Alloys Compd. 736 (2018) 332–339.

[39] C.R. Ravikumar, P. Kotteeswaran, V.B. Raju, A. Murugan, M.S. Santosh, H.P. Nagaswarupa, S.C. Prashantha, M.R.A. Kumar, M.S. Shivakumar, Influence of zinc additive and pH on the electrochemical activities of β-nickel hydroxide materials and its applications in secondary batteries, J. Ener. Stor. 9 (2017) 12–24.